Journal of
Synchrotron Radiation

ISSN 1600-5775

Received 14 October 2014
Accepted 2 December 2014

New methods in time-resolved Laue pump–probe crystallography at synchrotron sources

Philip Coppens* and Bertrand Fournier*

Chemistry Department, University at Buffalo, State University of New York, Buffalo, NY 14260-3000, USA. *E-mail: coppens@buffalo.edu, betrandf@buffalo.edu

Newly developed methods for time-resolved studies using the polychromatic and in particular the pink-Laue technique, suitable for medium and small-size unit cells typical in chemical crystallography, are reviewed. The order of the sections follows that of a typical study, starting with a description of the pink-Laue technique, followed by the strategy of data collection for analysis with the RATIO method. Novel procedures are described for spot integration, orientation matrix determination for relatively sparse diffraction patterns, scaling of multi-crystal data sets, use of Fourier maps for initial assessment and analysis of results, and least-squares refinement of photo-induced structural and thermal changes. In the calculation of Fourier maps a ground-state structure model, typically based on monochromatic results, is employed as reference, and the laser-ON structure factors for the Fourier summations are obtained by multiplying the reference ground-state structure factors by the square root of the experimental ON/OFF ratios. A schematic of the procedure followed is included in the conclusion section.

Keywords: photocrystallography; pink-Laue; orientation matrix determination; spot integration; multicrystal data sets.

1. Introduction

Structural dynamics is a field of crucial importance if we are to understand the course of chemical reactions and improve our ability to fine-tune important processes including catalysis, light emission and solar energy capture. The detailed knowledge of the geometric structure of short-lived species remains a key component for our understanding of dynamic processes in a broad range of fields including not only chemistry but also materials science and biology.

The synchrotron pump–probe technique has been pioneered in biomolecular crystallography (see, for example, Ren *et al.*, 1999; Moffat, 2001, 2003; Šrajer *et al.*, 2000; Schmidt, 2008). We here review recently developed methods designed for atomic-resolution synchrotron Laue experiments and subsequent analysis of photo-induced species of importance in chemistry and materials science. Although the methods discussed have been developed specifically for Laue experimentation, some are likely to be relevant for other types of time-resolved (TR) experiments including those at X-ray free-electron laser (XFEL) sources.

2. The pink-Laue technique

Both monochromatic and polychromatic Laue methods have been employed for TR studies at synchrotron sources. The advantage of the Laue methods is the broader energy range of the beam used, compared with a narrow beam from a perfect silicon monochromator, which results in a large increase of intensity. In the pink-Laue method (Bourgeois *et al.*, 2000, 2007; Ren *et al.*, 1999), as implemented at the BIOCARS ID-14 station at the Advanced Photon Source, the energy range is restricted to a bandwidth of $\sim\pm0.7$ keV, as shown in Fig. 1. The use of Laue methods eliminates the need for the thou-

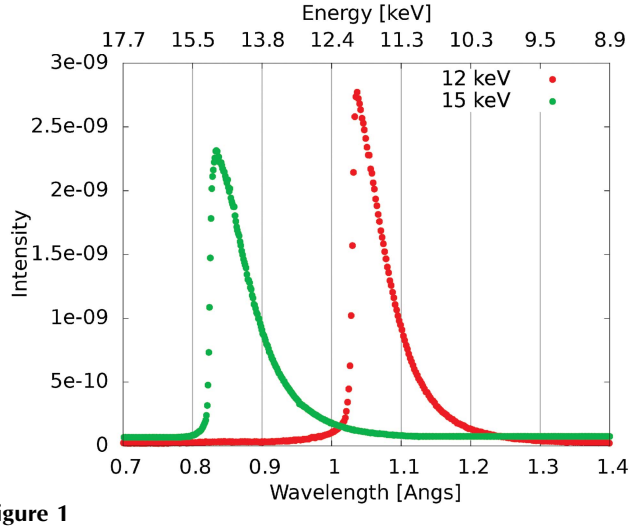

Figure 1
Intensity *versus* wavelength and energy ranges for two different settings at the BIOCARS 14-ID beamline at the Advanced Photon Source.

sands of pump–probe cycles required in the stroboscopic method typically used for monochromatic data collection (Coppens *et al.*, 2005). The laser-induced damage in the sample as well as a quite pronounced temperature increase due to the exposure are therefore considerably reduced. In a favorable case a single synchrotron pulse has been sufficient for recording a suitable diffraction pattern (Benedict *et al.*, 2011). In others, several pump–probe cycles are used before detector read-out.

Two specific problems must be addressed. In macromolecular crystallography the 'λ-curve' used for the wavelength-dependence correction of the intensity data prior to further processing is determined by fitting of the intensities of equivalent reflections scattered by different wavelengths with a many-term Chebyshev polynomial (Šrajer *et al.*, 2000; Ren & Moffat, 1995). Since the diffraction pattern tends to be much less dense in chemical-crystallographic experiments on smaller unit-cell samples, and the redundancy therefore much lower, this method is not feasible here. It is avoided by use of the RATIO method in which the analysis is based on the ratio of the laser-ON and laser-OFF intensities. This method is discussed in §3. The second issue concerns the steep slope of the wavelength distribution on its high-energy side in the pink-Laue spectrum, as shown in Fig. 1. A small change in unit-cell dimensions on exposure can lead to anomalous values of the ON/OFF ratios of reflections scattered by wavelengths in this narrow region, as any changes in cell dimensions on excitation will affect the wavelength at which a certain reflection is recorded. The effect is small when the conversion percentage and temperature increase are small, which is often also of importance to maintain the integrity of the crystal lattice. The affected reflections can be recognized in the subsequent analysis of equivalent reflections and confirmed by calculation of the wavelength from the observed Bragg angle and the *hkl* values available after indexing, and subsequently removed from the averaging procedure.

3. The RATIO method for data collection

The most sensitive measure of the structural change on excitation is the change in the intensity of each of the reflections. In the RATIO method (Coppens *et al.*, 2009) this is exploited by using the ON/OFF ratios as the observations in the light-exposed structure refinement with the program *LASER* (Vorontsov *et al.*, 2010), specifically designed for this purpose. As described above, a major advantage of the RATIO method when used with the Laue technique is elimination of the need to use a spectral curve to determine the wavelength at which each of the reflections is recorded. To fully exploit the use of the method, the laser-ON and laser-OFF intensities of each reflection should be collected immediately following each other. This eliminates longer range fluctuations in X-ray beam intensity, effects of slow sample deterioration, and differences in absorption corrections which would occur if laser-ON and laser-OFF reflections are collected at different times in different settings. It does not require relative scaling as the paired frames are collected at the same temperature in exactly the same setting and same conditions of the sample. As described in the following section, to increase the accuracy and allow estimate of experimental uncertainties, each ON/OFF pair is collected up to ten times at the same angular settings.

4. Integration strategies

In the conventional Laue data processing procedures the positions of the reflections on the detector are predicted from a known orientation matrix and a box is drawn which encloses the area where the diffraction signal is expected. Subsequent integration of the identified spots is performed either by two-dimensional profile fitting (Helliwell *et al.*, 1989; Šrajer *et al.*, 2000; Moffat, 2001) or by selecting a mask on the detector surface using statistical criteria as in the seed-skewness method (Bolotovsky & Coppens, 1997; Bolotovsky *et al.*, 1995). Although the latter does not in principle require information on the predicted spot position, the practical implementation of the method relies heavily on this information (Messerschmidt & Tschentscher, 2008). As available methods for determining the orientation of the Laue pattern are time-consuming and not always successful for all but dense diffraction patterns, a different procedure has been developed which does not require knowledge of the sample orientation, but allows real-time analysis of the statistical reproducibility of the intensities.

As part of the *LAUEUTIL* toolkit, a new spot-integration method, not requiring prior indexing of the reflections, was implemented (Kalinowski *et al.*, 2012). The first step is the estimation of the background. The estimate is obtained by statistical analysis along each of the pixel-lines, shown in Fig. 2. For a dark data set which consists of a series of laser-OFF frames, the background sample is assumed to be a constant fraction, typically the smallest 75% of all pixel counts on each of the lines (Fig. 3). As measurements of the TR data sets are

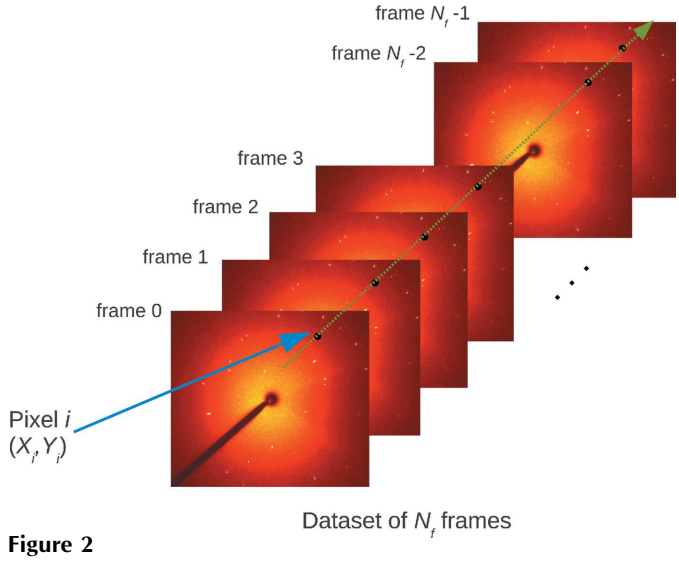

Figure 2
Collection of the profile along a single pixel-line. Reproduced from Kalinowski *et al.* (2012).

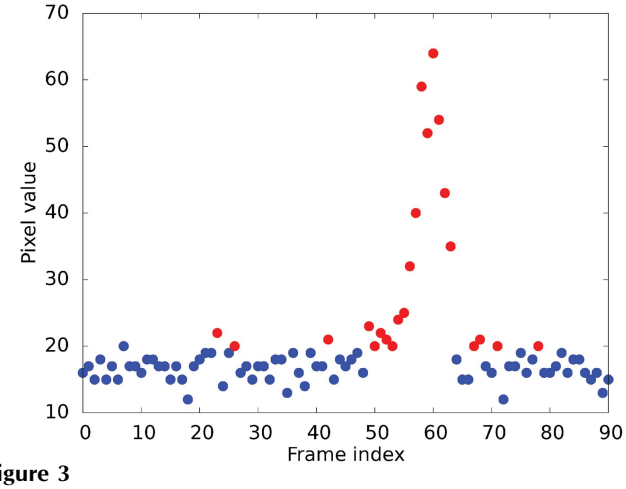

Figure 3
Intensities for one pixel on successive frames (ground state). A single frame was measured at each setting, 1° step scan. Red spots assigned as part of a peak, blue spots background. CuI(phenanthroline)$(PPh_3)_2$][BF_4]. Data from Makal *et al.* (2012). Modified from Kalinowski *et al.* (2012).

fast, each of the ON/OFF pairs of frames is collected up to ten times, together forming a *block* of up to 20 frame measurements at identical angle settings. A succession of values along a pixel-line in *blocks* of 20 measurements (10 ON and 10 OFF) is shown in Fig. 4. The two examples of pixel-line plots are selected at relatively low order. The first case (Fig. 4*a*) contains a large number of consecutive blocks of counts contributing to the diffraction spot. The second case (Fig. 4*b*) shows two distinct and in comparison weak reflections. We note that the fluctuation between the laser-ON and laser-OFF frames is not obvious before averaging of the repeated measurements. The sophisticated non-parametric Kruskal–Wallis statistical test (Kruskal & Wallis, 1952; Corder & Foreman, 2009) is used for distinguishing between diffraction peak and background blocks, shown in red and blue, respectively. Statistical properties of the background are estimated per pixel-line using values identified as background contribution. In a second step, on each frame the pixels with significant counts compared with the background are selected as potential parts of the diffraction spots.

The resulting logical array is referred to as a frame mask. The boundaries of the selected pixel clusters in the frame mask are represented in black in Fig. 5(*a*). For each frame a morphological analysis is performed (Kalinowski *et al.*, 2012). First, an erosion operation is applied to remove isolated pixels (represented by open squares in Fig. 5), and pixels on the periphery of the mask are removed; the remaining pixels after one erosion are represented by blue pixels in Fig. 5(*b*) (Jones *et al.*, 2001), and then two layers of peripheral pixels are added in two successive dilation

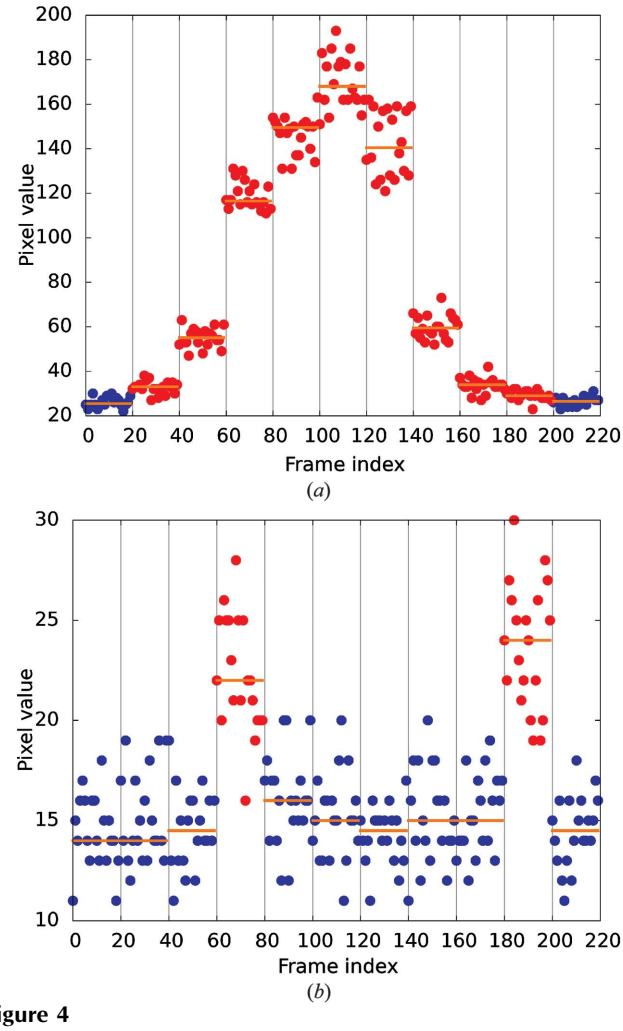

Figure 4
Two examples of pixel count plots for repeated measurements in each of 11 blocks of 20 frames (10 × ON/OFF) at each angular setting, 1° step scan. The blue dotted blocks are assigned as background by the Kruskal–Wallis statistical method. CuI(phenanthroline)$(PPh_3)_2$][BF_4]. Data from Makal *et al.* (2012). Modified from Kalinowski *et al.* (2012).

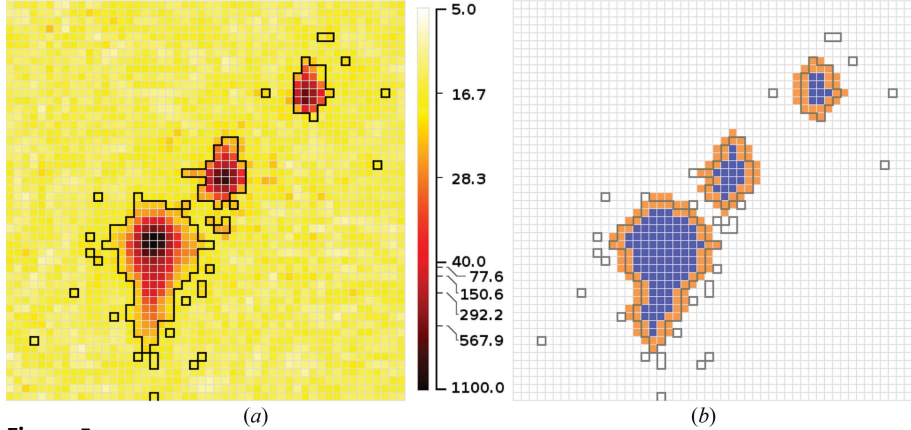

Figure 5
Morphological treatment of the spot masks on a frame after analysis of the counts along the pixel lines. (*a*) Pixel intensity in color with the boundaries of the originally selected pixel clusters in black. (*b*) Boundaries of the originally selected pixel clusters in grey, pixels remaining in the mask after erosion in blue and pixels added by two successive dilations in orange. The resulting mask of reflections after morphological operations is the union of orange and blue pixels. From Kalinowski *et al.* (2012).

operations (orange pixels in Fig. 5*b*) to produce the footprints of the reflections. The numbers of erosion and dilation operations are optional. Dilation operations are required to compensate the suppression of pixels at the periphery of pixel clusters and avoid underestimation of spot footprints. The final result for three adjacent reflections on a frame is shown in Fig. 5(*b*) by the blue and orange pixels. In the final procedure a common footprint can be assigned to all laser-ON and laser-OFF recordings of a reflection on successive frames, using OR logic, *i.e.* if a pixel is included in any of the frames it is accepted. The diffraction reflection intensities are calculated by summation of the pixel counts over the footprints after subtraction of the background.

ON/OFF intensity ratios in each of the pairs in a block are subsequently averaged, and standard deviations are estimated based on the spread in ratio values in a block. The method requires neither prior assumptions such as fitting of a profile, definition of an integration box or assignment of Miller indices to recognize maxima. It is thus orientation-matrix independent. One of its significant advantages is that it is rapid and therefore allows comparison of intensity changes in data sets collected more than once in real time, while subsequent data are being collected.

5. Orientation matrix determination

Methods developed for orientation matrix determination of a macromolecular diffraction pattern typically make use of nodal spots, representing prominent zones, recognizable from the intersection of well populated arcs formed by the reflections, as implemented in the Daresbury program *LAUEGEN* (Helliwell *et al.*, 1989) and adopted in subsequently written software. The method is not suitable for sparsely populated patterns, which occur for medium-size unit cells. A different procedure is therefore adopted, based on comparison of the angles between pairs of central reciprocal lattice rays of strong reflections in the synchrotron set and pairs in the reference monochromatic data. The different orientations of the reference and experimental sets are illustrated for the case of tetragonal [Cu_4I_4(piperidine)$_4$] (Kaminski *et al.*, 2010) in Fig. 6 (Kalinowski *et al.*, 2011). If a match of angles is found, the corresponding rotation matrix, defining a potential relation between the known orientation of the monochromatic set and the orientation of the crystal being studied, is saved and recorded in the Euler space of the three rotation angles. The correct rotation matrix is recognized by a large clustering of spots in this space. The procedure has been encoded in the *LAUEUTIL* toolkit. Further details can be found in the relevant reference (Kalinowski *et al.*, 2011). The method uses the whole data set rather than single frames as in the node-recognition technique. It should be noted that the comparison with monochromatic data was applied on a much smaller scale in earlier work (Hart & Rietman, 1982; Laughier & Filhol, 1983).

Figure 6
Visualization of projections of points in reciprocal space on a unit sphere. Left: monochromatic data; eight equivalent asymmetric units in reciprocal space are represented with different colors. Right: points from a Laue data set. [Reproduced from Kalinowski *et al.* (2011).]

6. Scaling of multi-crystal ratio data sets

Scaling of data sets collected on different specimens is a necessary step prior to the calculation of the Fourier maps discussed in the following section. It is also necessary if a merged data set is to be used to refine a structural model by the least-squares method, although the program *LASER* allows refinement of separate data sets with individual ratio scale factors, excited-state (ES) populations and separate temperature scale parameters, as discussed in §8.

6.1. Absolute η scaling

The simplest scaling is based on the fractional change of each of the reflections on light exposure, defined as

$$\eta(\mathbf{H}) = \frac{I(\mathbf{H})^{\text{laserON}} - I(\mathbf{H})^{\text{laserOFF}}}{I(\mathbf{H})^{\text{laserOFF}}} = R(\mathbf{H}) - 1, \qquad (1)$$

in which $I(\mathbf{H})$ is the intensity of a reflection with reciprocal lattice vector $\mathbf{H}$.

The scaling by this method is based on the *average absolute system response* (AARS) derived from the $|\eta|$ values of the unique reflections after merging:

$$\eta^{i}_{\text{obs,scaled}}(\mathbf{H}) = \frac{\langle|\eta_{\text{obs}}(\mathbf{H})|\rangle_{\text{all sets } i}}{\langle|\eta_{\text{obs}}(\mathbf{H})|\rangle_{\text{set } i}} \times \eta^{i}_{\text{obs}}(\mathbf{H}). \qquad (2)$$

The method is based on two assumptions. The first is that the effect of the laser-induced temperature increase, expressed by the isotropic global thermal-motion increase parameter ΔB or the temperature scale factor k_{B}, multiplying the ground-state anisotropic or isotropic thermal parameters, and the population of the excited state P are proportional. The second implicit assumption is that all data sets share the same set of unique reflections. This is not a strict limitation as long as the data sets share a significant number of common reflections.

6.2. Weighted least-squares scaling

This more sophisticated scaling method involves weighted least-squares, without consideration of excited-state structural models, against all observed ratios to obtain a single set of scaled ratios. It follows methods first introduced by Hamilton *et al.* (1965) and Fox & Holmes (1966) and implemented by

Blessing in the *SORTAV* program (Blessing, 1997), but here applied to the observed ratios.

The error function minimized is

$$\varepsilon^{R}_{\min} = \sum_{\text{all sets}} \sum_{\text{all } \mathbf{H} \text{ in set } i} \sum_{\text{all obs } (\mathbf{H}) \text{ in set } i} w^{i,j}_{\text{obs}} \times (\mathbf{H})\left[R^{i,j}_{\text{obs}}(\mathbf{H}) - R^{i}_{\text{model}}(\mathbf{H})\right]^2, \quad (3)$$

in which $R^{i,j}_{\text{obs}}(\mathbf{H})$ and $R^{i}_{\text{model}}(\mathbf{H})$ represent, respectively, the jth observed ratio value and the model ratio of reflection H in set i. The minimization requires the parameterization of the ratios R. They are written as a product of the structural and thermal contributions, $S^{i}_{\text{model}}(\mathbf{H})$ and $T^{i}_{\text{model}}(\mathbf{H})$, respectively:

$$R^{i}_{\text{model}}(\mathbf{H}) = S^{i}_{\text{model}}(\mathbf{H})\, T^{i}_{\text{model}}(\mathbf{H}) \quad (4)$$

with

$$S^{i}_{\text{model}}(\mathbf{H}) = P^{i} L_{\text{model}}(\mathbf{H}) + 1. \quad (5)$$

$L_{\text{model}}(\mathbf{H})$ is the structural change for 100% conversion, expressions for which have been reported earlier (Fournier & Coppens, 2014*b*). They depend on the distribution of the excited-state species, for which two models have been defined, corresponding to a random distribution (RD model) or formation of clusters of excited-state molecules (CF model) (Vorontsov & Coppens, 2005). If the relative ES population of data set i is defined as $Q^{i} = P^{i}/\langle P^{i}\rangle_{\text{all sets}}$ we obtain

$$\eta^{\Delta T=0}_{\text{model}}(\mathbf{H}) = \langle P^{i}\rangle_{\text{all sets}}\, L_{\text{model}}(\mathbf{H}), \quad (6)$$

then expression (5) can be rewritten as

$$S^{i}_{\text{model}}(\mathbf{H}) = Q^{i} \eta^{\Delta T=0}_{\text{model}}(\mathbf{H}) + 1.$$

As described in §6.1, the thermal contribution $T_{\text{model}}(\mathbf{H})$ is a function of either the isotropic thermal-motion increase parameter ΔB or the anisotropic thermal-motion scale factor k_{B}.

In the case of relatively small ES percentages ($\sim$<10%), and therefore small thermal effects, which are typical for most studies if crystal breakdown is to be avoided, we obtain

$$T^{i,\Delta B}_{\text{model}}(\mathbf{H}) = \exp\left[-2\Delta B^{i} s^{2}(\mathbf{H})\right] \simeq 1 - 2\Delta B^{i} s^{2}(\mathbf{H}), \quad (7)$$

with $s = \sin\theta/\lambda$.

If we define the Q-normalized increase in ΔB^{i} as $(\Delta B^{i})/Q^{i}$, then the average over all sets becomes

$$A_{\Delta B_Q} = \left\langle \frac{\Delta B^{i}}{Q^{i}} \right\rangle_{\text{all sets}}, \quad (8)$$

and the modeled value of η of the reflection $\mathbf{H}$ will be

$$\eta^{\Delta B}_{\text{model}}(\mathbf{H}) = \eta^{\Delta T=0}_{\text{model}}(\mathbf{H}) - 2A_{\Delta B_Q} s^{2}(\mathbf{H}), \quad (9)$$

while, for each data set i,

$$\delta\Delta B^{i}_{Q} = \frac{\Delta B^{i}}{Q^{i}} - A_{\Delta B_Q}(\mathbf{H}) \quad (10)$$

to give

$$R^{i,\Delta B}_{\text{model}}(\mathbf{H}) \simeq 1 + Q^{i}\left[\eta^{\Delta T=0}_{\text{model}}(\mathbf{H}) - 2\delta\Delta B^{i}_{Q}\, s^{2}(\mathbf{H})\right]. \quad (11)$$

Similar expressions have been derived for the thermal model based on the temperature scale factor k_{B} (Fournier & Coppens, 2014*b*).

Summarizing, the observations in this weighted least-squares refinement are the ratios collected from each block, with as variables the $\eta_{\text{model}}(\mathbf{H})$ for each unique reflection $\mathbf{H}$, the relative excited state population parameters Q^{i} and the temperature increase variables $\delta\Delta B^{i}_{Q}$ or δk^{i}_{B} for each of the data sets. In the case where the laser-ON and laser-OFF frames have not been collected in sequence but in separate runs, in addition the ratio of the scale factors of the laser-ON and laser-OFF sets have to be included as variables (Fournier & Coppens, 2014*b*).

7. The use of Fourier maps for initial evaluation, monitoring the refinement and final analysis

Three different types of Fourier maps can be used in photocrystallography; they are photodifference maps, residual maps and photodeformation maps (Fournier & Coppens, 2014*a*). Calculation of the maps requires scaling as discussed in the previous section if multi-crystal data sets are to be used. Examples of photodifference and photodeformation maps are given in Figs. 7 and 8.

7.1. Photodifference maps

It has become common in photocrystallographic studies to obtain an initial estimate of the induced change by calculation of a photodifference Fourier map, based on the difference between the observed laser-ON and laser-OFF structure factors (Coppens *et al.*, 2008; Collet *et al.*, 2012; Makal *et al.*, 2011). The map is defined by

$$\begin{aligned}\Delta\rho(\mathbf{r}) &= \rho^{\text{laserON}}_{\text{obs}}(\mathbf{r}) - \rho^{\text{laserOFF}}_{\text{obs}}(\mathbf{r}) \\ &= (1/V)\sum_{\mathbf{H}}\left[F^{\text{laserON}}_{\text{obs}}(\mathbf{H}) - F^{\text{laserOFF}}_{\text{obs}}(\mathbf{H})\right] \\ &\quad \times \exp\left[i\varphi^{\text{laserOFF}}_{\text{calc}}(\mathbf{H})\right]\exp(-i2\pi\mathbf{H}\cdot\mathbf{r}), \end{aligned} \quad (12)$$

in which ρ is the density, and F and φ are, respectively, the amplitude of the structure factor and the phase of the reflection $\mathbf{H}$. The equation assumes no change in phase on excitation, which is a very good approximation for centrosymmetric structures when conversion percentages are low.

When the RATIO method is used and a monochromatic ground-state structure is available, this expression can be rewritten by the definition of a 'semi-observed' laser-ON-structure factor, defined as

$$F^{\text{laserON}}_{\text{semi-obs}}(\mathbf{H}) = \left[R_{\text{obs}}(\mathbf{H})^{1/2}\, F^{\text{reference}}_{\text{calc}}(\mathbf{H})\right], \quad (13)$$

in which $F^{\text{reference}}_{\text{calc}}(\mathbf{H})$ is based on the independent atom model (IAM), leading to

$$\begin{aligned}\Delta\rho(\mathbf{r}) &= (1/V)\sum_{\mathbf{H}}[R_{\text{obs}}(\mathbf{H})^{1/2} - 1]\, F^{\text{reference}}_{\text{calc}}(\mathbf{H}) \\ &\quad \times \exp\left[i\varphi^{\text{reference}}_{\text{calc}}(\mathbf{H})\right]\exp(-i2\pi\mathbf{H}\cdot\mathbf{r}). \end{aligned} \quad (14)$$

The errors in the resulting photodifference map are mainly due to the errors in the ratios from the Laue synchrotron

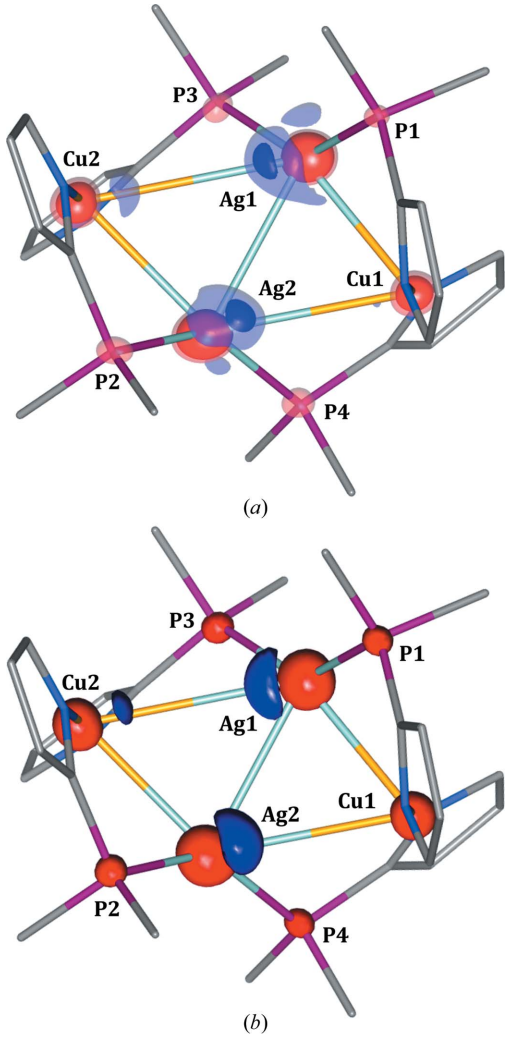

Figure 7
(*a*) Photodifference map of a complex with an Ag_2Cu_2 core. Isosurfaces at 0.55 and 0.35. (*b*) Photodeformation map (defined in §7.3) based on the refined model parameters. Blue positive, red negative. (Isosurfaces, ± 0.30 e Å^{-3}; blue, positive; red, negative; $k_B = 1.06$.) [Jarzembska *et al.* (2014). Reprinted with permission from *Inorg. Chem.* (2014), **53**, 10594–10601, Copyright 2014 American Chemical Society.]

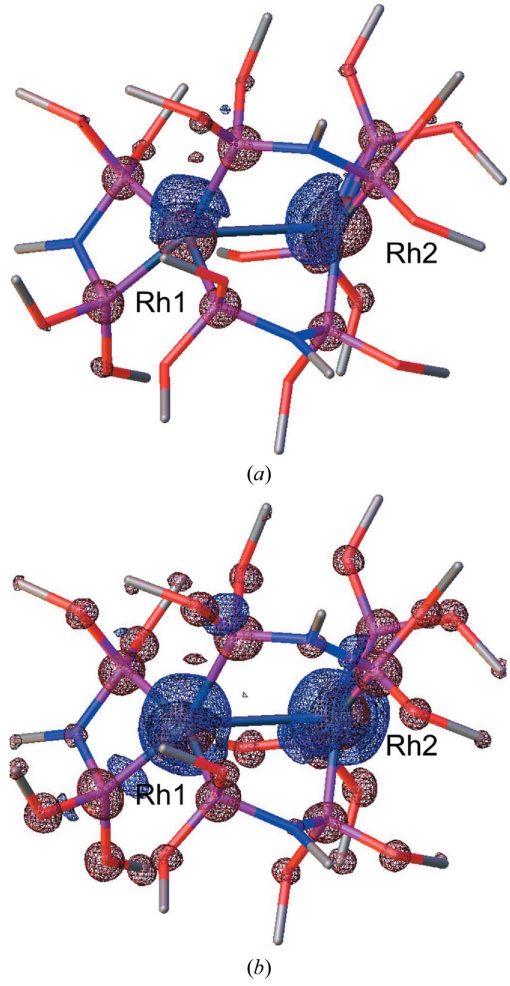

Figure 8
Three-dimensional photodeformation maps of $Rh_2(\mu\text{-PNP})_2(PNP)_2(BPh_4)2$ {PNP = $CH_3N[P(OCH_3)_2]_2$, Ph = phenyl} with isosurfaces of 0.25 e Å^{-3}. (*a*) Observed *hkl*s only; (*b*) all *hkl*s with maximal experimental resolution of 0.5317 Å^{-1}, showing also shifts of the lighter P atoms. [Reproduced from Makal *et al.* (2011); Fournier & Coppens (2014*a*).]

experiment, as the monochromatic data are typically highly accurate.

7.2. Residual maps.

Residual maps are a powerful tool to monitor the progress of a refinement and judge its success after refinement has been completed. They are defined as

$$\Delta\rho(\mathbf{r}) = (1/V)\sum_{\mathbf{H}}\left[R_{\rm obs}(\mathbf{H})^{1/2}\,F_{\rm calc}^{\rm reference}(\mathbf{H}) - F_{\rm calc}^{\rm laserON}(\mathbf{H})\right] \times \exp\left[i\varphi_{\rm calc}^{\rm laserON}(\mathbf{H})\right] \times \exp(-i2\pi\mathbf{H}\cdot\mathbf{r}). \quad (15)$$

7.3. Photodeformation maps

Photodeformation maps are plotted to illustrate the light-induced changes according to the converged refinement model. They are calculated from the difference between the laser-ON and reference laser-OFF IAM electron-density distributions, as follows:

$$\Delta\rho(\mathbf{r}) = 1/V\sum_{\mathbf{H}}\left\{F_{\rm calc}^{\rm laserON}(\mathbf{H})\exp\left[i\varphi_{\rm calc}^{\rm laserON}(\mathbf{H})\right] - F_{\rm calc}^{\rm reference}(\mathbf{H})\exp\left[i\varphi_{\rm calc}^{\rm reference}(\mathbf{H})\right]\right\} \times \exp(-i2\pi\mathbf{H}\cdot\mathbf{r}). \quad (16)$$

If desired, the maps can be calculated at a resolution beyond that achieved in the Laue experiment, for example with all the reflections measured in the monochromatic experiment. Also, thermal differences between the laser-ON and laser-OFF data sets can be eliminated in the calculation (Fournier & Coppens, 2014*b*). Two examples are shown in Fig. 8. The maps may be compared with model maps used extensively in X-ray charge density analysis for several decades (Hirshfeld, 1971; Harel & Hirshfeld, 1975).

8. The RATIO method for excited-state structure refinement and agreement factors

8.1. Agreement factors

R-factors for dynamic structure crystallography can be based either on the ratios of the reflections or on the fractional intensity changes defined earlier as

$$\eta(\mathbf{H}) = \frac{I(\mathbf{H})^{\text{laserON}} - I(\mathbf{H})^{\text{laserOFF}}}{I(\mathbf{H})^{\text{laserOFF}}} = R(\mathbf{H}) - 1,$$

to give

$$\mathcal{R}_1(R) = \frac{\sum_{\mathbf{H}} \left| R_{\text{obs}}(\mathbf{H}) - R_{\text{calc}}(\mathbf{H}) \right|}{\sum_{\mathbf{H}} \left| R_{\text{obs}}(\mathbf{H}) \right|} \tag{17}$$

and

$$\mathcal{R}_1(\eta) = \frac{\sum_{\mathbf{H}} \left| \eta_{\text{obs}}(\mathbf{H}) - \eta_{\text{calc}}(\mathbf{H}) \right|}{\sum_{\mathbf{H}} \left| \eta_{\text{obs}}(\mathbf{H}) \right|} \tag{18}$$

and analogous for the weighted R-factors.

The numerators of (17) and (18) are equal, but the sum of the observed $|\eta|$ values in the denominator is much smaller, so the η-based $\mathcal{R}$-factors will be much larger than the R-based ones. They are also strongly affected by the magnitude of the temperature increase, which may be different for data sets collected at different laser power, or on different samples. They are therefore not suited for comparison of the results on different data sets. It can be shown that the RATIO-based $\mathcal{R}$-factors tend to be larger but of the same order of magnitude as the I_{obs}-based $\mathcal{R}$-factors used in conventional crystallography (Coppens *et al.*, 2010; Fournier & Coppens, 2014*a*).

8.2. Least-squares refinement of ratio data

The program *LASER* is based on the refinement of the ratios of the observed intensities, rather than the structure factors. An earlier version (Vorontsov *et al.*, 2010) has now been modified. Both versions allow simultaneous refinement against up to six data sets on the same structure with separate populations, structural and thermal parameters, or, alternatively, refinement against a scaled data set of unique reflections. Variables are atomic structural parameters, rotations and translations of rigid bodies plus population P and thermal k_{B} parameters of either each of the individual data sets or a merged data set after scaling.

9. Concluding remarks

The above represents an overview of methods developed in recent years for the use of an extended energy range of the X-rays generated by synchrotron sources. A scheme of the procedure and choices to be made is shown in Fig. 9.

The methods have been applied to several data sets. The recent study of the Ag_2Cu_2 complex (Jarzembska *et al.*, 2014) illustrates how reasonable accurate results on the excited-state structures can be obtained even at small conversion percentages. Some aspects discussed are relevant for use with 'diffract and destroy' methods at synchrotron sources. Many also apply to monochromatic in-house time-resolved diffraction, which is currently being developed (Kaminski *et al.*, 2014*a*,*b*). Software has been made available at the Workshop on Dynamic Structural Crystallography, which took place in June 2013 (Trzop & Jarzembska, 2013). Updated versions will be released on the web in the near future.

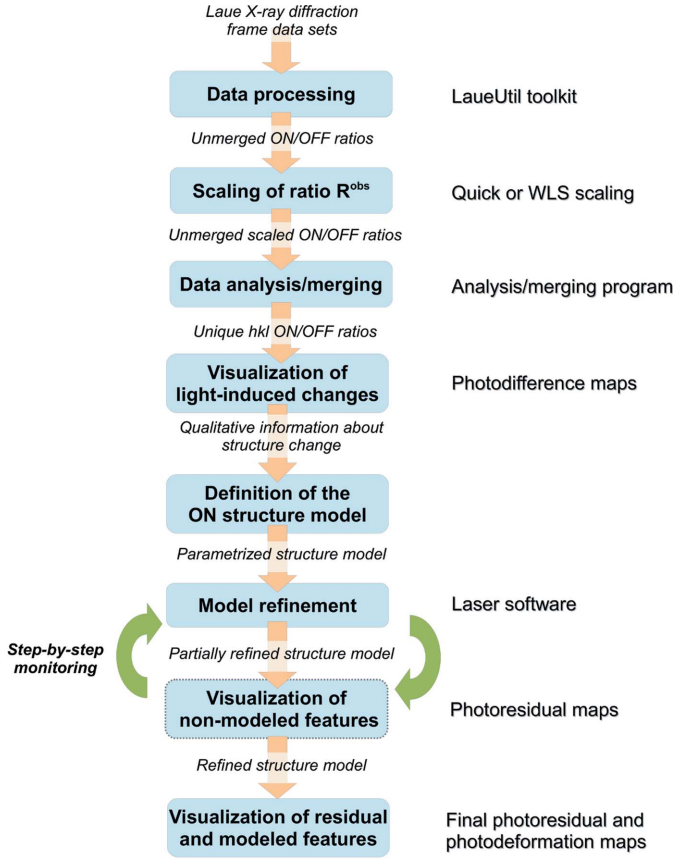

Figure 9
Schematic of options in data collection, relative scaling and refinement.

Research funded by the National Science Foundation (CHE1213223). The BioCARS Sector 14 is supported by the National Institutes of Health, National Center for Research Resources (RR007707). The APS is sponsored by the US Department of Energy, Office of Basic Energy Sciences (W-31-109-ENG-38).

References

Benedict, J. B., Makal, A., Sokolow, J. D., Trzop, E., Scheins, S., Henning, R., Graber, T. & Coppens, P. (2011). *Chem. Commun.* **47**, 1704–1706.
Blessing, R. H. (1997). *J. Appl. Cryst.* **30**, 421–426.
Bolotovsky, R. & Coppens, P. (1997). *J. Appl. Cryst.* **30**, 244–253.
Bolotovsky, R., White, M. A., Darovsky, A. & Coppens, P. (1995). *J. Appl. Cryst.* **28**, 86–95.
Bourgeois, D., Schotte, F., Brunori, M. & Vallone, B. (2007). *Photochem. Photobiol. Sci.* **6**, 1047–1056.
Bourgeois, D., Wagner, U. & Wulff, M. (2000). *Acta Cryst.* D**56**, 973–985.
Collet, E., Moisan, N., Baldé, C., Bertoni, R., Trzop, E., Laulhé, C., Lorenc, M., Servol, M., Cailleau, H., Tissot, A., Boillot, M.-L.,

Graber, T., Henning, R., Coppens, P. & Buron-Le Cointe, M. (2012). *Phys. Chem. Chem. Phys.* **14**, 6192–6199.
Coppens, P., Kamiński, R. & Schmøkel, M. S. (2010). *Acta Cryst.* A**66**, 626–628.
Coppens, P., Pitak, M., Gembicky, M., Messerschmidt, M., Scheins, S., Benedict, J., Adachi, S., Sato, T., Nozawa, S., Ichiyanagi, K., Chollet, M. & Koshihara, S. (2009). *J. Synchrotron Rad.* **16**, 226–230.
Coppens, P., Vorontsov, I. I., Graber, T., Gembicky, M. & Kovalevsky, A. Y. (2005). *Acta Cryst.* A**61**, 162–172.
Coppens, P., Zheng, S.-L. & Gembicky, M. (2008). *Z. Kristallogr.* **223**, 265–271.
Corder, G. W. & Foreman, D. I. (2009). *Nonparametric Statistics for Non-Statisticians: A Step-by-Step Approach.* Hoboken: Wiley.
Fournier, B. & Coppens, P. (2014*a*). *Acta Cryst.* A**70**, 291–299.
Fournier, B. & Coppens, P. (2014*b*). *Acta Cryst.* A**70**, 514–517.
Fox, G. C. & Holmes, K. C. (1966). *Acta Cryst.* **20**, 886–891.
Hamilton, W. C., Rollett, J. S. & Sparks, R. A. (1965). *Acta Cryst.* **18**, 129–130.
Harel, M. & Hirshfeld, F. L. (1975). *Acta Cryst.* B**31**, 162–172.
Hart, H. V. & Rietman, E. A. (1982). *J. Appl. Cryst.* **15**, 126–129.
Helliwell, J. R., Habash, J., Cruickshank, D. W. J., Harding, M. M., Greenhough, T. J., Campbell, J. W., Clifton, I. J., Elder, M., Machin, P. A., Papiz, M. Z. & Zurek, S. (1989). *J. Appl. Cryst.* **22**, 483–497.
Hirshfeld, F. L. (1971). *Acta Cryst.* B**27**, 769–781.
Jarzembska, K., Kamiński, R., Fournier, B., Trzop, E., Sokolow, J., Henning, R., Chen, Y. & Coppens, P. (2014). *Inorg. Chem.* **53**, 10594–10601.
Jones, E., Oliphant, E., Peterson, P. *et al.* (2001). *SciPy*, http://www.scipy.org/.
Kalinowski, J. A., Fournier, B., Makal, A. & Coppens, P. (2012). *J. Synchrotron Rad.* **19**, 637–646.
Kalinowski, J. A., Makal, A. & Coppens, P. (2011). *J. Appl. Cryst.* **44**, 1182–1189.
Kaminski, R., Benedict, J., Trzop, E., Jarzembska, K., Fournier, B. & Coppens, P. (2014a). *Acta Cryst.* A**70**, C775.
Kamiński, R., Graber, T., Benedict, J. B., Henning, R., Chen, Y.-S., Scheins, S., Messerschmidt, M. & Coppens, P. (2010). *J. Synchrotron Rad.* **17**, 479–485.
Kamiński, R., Nottingham, G. & Coppens, P. (2014b). *J. Appl. Cryst.* **47**, 1765–1768.
Kruskal, W. H. & Wallis, W. A. (1952). *J. Am. Stat. Assoc.* **47**, 583–621.
Laughier, J. & Filhol, A. (1983). *J. Appl. Cryst.* **16**, 281–283.
Makal, A., Benedict, J., Trzop, E., Sokolow, J., Fournier, B., Chen, Y., Kalinowski, J. A., Graber, T., Henning, R. & Coppens, P. (2012). *J. Phys. Chem. A*, **116**, 3359–3365.
Makal, A., Trzop, E., Sokolow, J., Kalinowski, J., Benedict, J. & Coppens, P. (2011). *Acta Cryst.* A**67**, 319–326.
Messerschmidt, M. & Tschentscher, T. (2008). *Acta Cryst.* A**64**, C611.
Moffat, K. (2001). *Chem. Rev.* **101**, 1569–1582.
Moffat, K. (2003). *Faraday Disc.* **122**, 65–77.
Ren, Z., Bourgeois, D., Helliwell, J. R., Moffat, K., Šrajer, V. & Stoddard, B. L. (1999). *J. Synchrotron Rad.* **6**, 891–917.
Ren, Z. & Moffat, K. (1995). *J. Appl. Cryst.* **28**, 461–481.
Schmidt, M. (2008). *Ultrashort Laser Pulses in Biology and Medicine*, edited by M. Braun, P. Gilch and W. Zinth, pp. 201–241. Berlin/Heidelberg: Springer.
Šrajer, V., Crosson, S., Schmidt, M., Key, J., Schotte, F., Anderson, S., Perman, B., Ren, Z., Teng, T., Bourgeois, D., Wulff, M. & Moffat, K. (2000). *J. Synchrotron Rad.* **7**, 236–244.
Trzop, E. & Jarzembska, K. (2013). *ACA RefleXions*, **3**, 66.
Vorontsov, I. I. & Coppens, P. (2005). *J. Synchrotron Rad.* **12**, 488–493.
Vorontsov, I., Pillet, S., Kamiński, R., Schmøkel, M. S. & Coppens, P. (2010). *J. Appl. Cryst.* **43**, 1129–1130.